IJMMM International Journal of Minerals, Metallurgy and Materials 矿物冶金与材料学报（英文版）

A functionalized activated carbon adsorbent prepared from waste amidoxime resin by modifying with H_3PO_4 and $ZnCl_2$ and its excellent Cr(VI) adsorption

Chunlin He, Yun Liu, Mingwei Qi, Zunzhang Liu, Yuezhou Wei, Toyohisa Fujita, Guifang Wang, Shaojian Ma, and Wenchao Yang

Cite this article as:
Chunlin He, Yun Liu, Mingwei Qi, Zunzhang Liu, Yuezhou Wei, Toyohisa Fujita, Guifang Wang, Shaojian Ma, and Wenchao Yang, A functionalized activated carbon adsorbent prepared from waste amidoxime resin by modifying with H_3PO_4 and $ZnCl_2$ and its excellent Cr(VI) adsorption, *Int. J. Miner. Metall. Mater.*, 31(2024), No. 3, pp. 585-598. https://doi.org/10.1007/s12613-023-2737-z

View the article online at SpringerLink or IJMMM Webpage.

INTERNATIONAL JOURNAL OF
Minerals, Metallurgy and Materials

Volume 31, Number 3, March 2024
Page 585

Research Article https://doi.org/10.1007/s12613-023-2737-z

A functionalized activated carbon adsorbent prepared from waste amidoxime resin by modifying with H_3PO_4 and $ZnCl_2$ and its excellent Cr(VI) adsorption

Chunlin He[1,2,5),✉], *Yun Liu*[1,2)], *Mingwei Qi*[1,2)], *Zunzhang Liu*[1,2)], *Yuezhou Wei*[3,4)], *Toyohisa Fujita*[1,2)], *Guifang Wang*[1,2)], *Shaojian Ma*[1,2)], *and Wenchao Yang*[1,2)]

1) School of Resources, Environment and Materials, Guangxi University, Nanning 530004, China
2) State Key Laboratory of Featured Metal Materials and Life-cycle Safety for Composite Structures, Guangxi University, Nanning 530004, China
3) School of Nuclear Science and Technology, University of South China, Hengyang 421000, China
4) School of Nuclear Science and Engineering, Shanghai Jiao Tong University, Shanghai 200240, China
5) Key Laboratory of New Low-carbon Green Chemical Technology, Education Department of Guangxi Zhuang Autonomous Region, Nanning 530004, China
(Received: 10 April 2023; revised: 30 June 2023; accepted: 8 September 2023)

Abstract: With the application of resins in various fields, numerous waste resins that are difficult to treat have been produced. The industrial wastewater containing Cr(VI) has severely polluted soil and groundwater environments, thereby endangering human health. Therefore, in this paper, a novel functionalized mesoporous adsorbent PPR-Z was synthesized from waste amidoxime resin for adsorbing Cr(VI). The waste amidoxime resin was first modified with H_3PO_4 and $ZnCl_2$, and subsequently, it was carbonized through slow thermal decomposition. The static adsorption of PPR-Z conforms to the pseudo-second-order kinetic model and Langmuir isotherm, indicating that the Cr(VI) adsorption by PPR-Z is mostly chemical adsorption and exhibits single-layer adsorption. The saturated adsorption capacity of the adsorbent for Cr(VI) could reach 255.86 mg/g. The adsorbent could effectively reduce Cr(VI) to Cr(III) and decrease the toxicity of Cr(VI) during adsorption. PPR-Z exhibited Cr(VI) selectivity in electroplating wastewater. The main mechanisms involved in the Cr(VI) adsorption are the chemical reduction of Cr(VI) into Cr(III) and electrostatic and coordination interactions. Preparation of PPR-Z not only solves the problem of waste resin treatment but also effectively controls Cr(VI) pollution and realizes the concept of "treating waste with waste".

Keywords: waste amidoxime resin; mesoporous adsorbent; H_3PO_4 and $ZnCl_2$ processing; Cr(VI) adsorption; electroplating wastewater

1. Introduction

Due to the large adsorption capacity, high adsorption selectivity, stable chemical properties, and insolubility in acids and alkalis [1–2], resins are widely used in water treatment, hydrometallurgy, biopharmaceutics [3], three-dimensional (3D) printing, coating [4], matrix for composites [5], etc. China is the leading producer of ion exchange resin in the world, producing a large amount of waste ion exchange resin or amidoxime chelating resin annually. For example, in the Guangxi branch of Chalco, amidoxime chelating resins utilized for gallium (Ga) adsorption from Bayer solution are discarded after reusing 50–60 times a month. After being reused many times, the resin (adsorbent) becomes waste resin. Moreover, its pore channel collapses and shrinks, specific surface area decreases, and functional group fails [2]. The natural degradation of the waste resin is challenging due to its stable properties. Hence, the resins are mainly treated through stacking, landfill, solidification [3,6], and incineration [7]. However, stacking and landfilling with waste resin require a large amount of land, and incineration generates air pollutants, such as CO, SO_2, NH_3, and NO_2 [8]. Amidoxime resin, one of the waste resins, is a type of chelating resin [1] with polystyrene as the main skeleton, while amino (–NH_2) and oxime (=N–OH) functional groups are connected to the same carbon atom. It is widely used in Guangxi, Henan, Shanxi, Guizhou, and other places in China. These waste amidoxime resins are sent to the solid waste treatment company for incineration at a cost of approximately $350 per ton [1–2]. Some researchers have focused on recycling waste resin (ion exchange resin). For instance, Peng *et al.* [9] prepared a new iron–carbon composite material by poisoning the waste resin with iron to remove phosphate from wastewater. Yang *et al.* [10] prepared superfine CeO_2 nanoparticles-modified porous carbon spheres with waste ion exchange resin to remove Cr(VI) from aqueous solution, where KOH activation and $Ce(NO_3)_3$ were used to modify the nanoparticle synthesis. The process was complex, and its cost was high. Moreover, the prepared adsorbent only had a small adsorption capacity for Cr(VI). In summary, many studies have focused on preparing activated carbon using ion exchange resin to recycle waste resin. However, amine oxime resin has not been stud-

✉ Corresponding author: Chunlin He E-mail: helink1900@126.com

ied systematically for this purpose till now. Therefore, the most ecofriendly, economical, and effective approach to solve the issues of waste amidoxime resin is to reuse it [11].

Furthermore, Cr(VI) and its compounds are widely used for synthesizing dye and pigment, processing leather, and in industries such as electroplating and metallurgy. If not effectively treated or controlled, a large number of chromium-containing products will pollute soil and groundwater environments significantly [12]. Cr(VI) can remain in soil and water for a long time [13], endangering human health by enriching the food chain. Cr mainly exists in wastewater in the form of Cr(VI) and Cr(III) [14], which have different chemical behavior and biological toxicity. Cr(III) is an auxiliary component for digesting glucose, lipids, and amino acids; hence, it can be used as a dietary enhancer. Additionally, Cr(VI) cannot be naturally degraded in wastewater and waste; therefore, it can easily accumulate in organisms and the human body and cause long-term harm [15]. The Cr(VI) toxicity is approximately 100 times more than that of Cr(III). Additionally, Cr(VI) is a highly toxic carcinogen and a severely corrosive medium. Therefore, if its concentration in water exceeds 0.1 mg/L, it will be toxic to the human body [16]. Furthermore, Cr(VI) intake by the human body will damage the nervous system, leading to dermatitis, renal failure, lung cancer, and even death [17]. In particular, heavy metal ions, such as chromium, cadmium, nickel, copper, and zinc, present in electroplating wastewater can severely pollute the water environment [18]. Several methods are available to remove Cr(VI) from an aqueous solution, including electrochemical reduction [19], chemical precipitation [19], solvent extraction [20], membrane separation [21], adsorption [19], and biological treatment [19]. Pavithra *et al.* [22] adopted a three-phase three-dimensional electric reactor. Electrocoagulation (combination of coagulation/flotation and electrochemistry) leads to the formation of a dynamic phase in the coagulant for removing Cr(VI) ions from wastewater. Kurniawan *et al.* [23] used Azotobacter s8, Bacillus subtilis, and Pseudomonas fetid to remove Cr(VI); here, Azotobacter s8 exhibited good potential for removing Cr(VI) from wastewater. However, this method is limited by the long bacterial culture cycle and removal environment, affecting its application on a large scale. Compared with other processing technologies, adsorption technology has the advantages of low cost, flexibility, simplicity, convenient operation, and high sensitivity, and it can avoid the formation of secondary pollutant waste [24–25]. Considering the adsorption capacity, the present research is focused on the selectivity of Cr(VI) and the performance stability of adsorbents after desorption. Due to the strong oxidizing nature of Cr(VI), functional groups often undergo oxidation during the adsorption and desorption processes. Although some studies have considered reducing Cr(VI) to Cr(III) (using oxalic acid) before adsorption to circumvent this problem, the cycling ability of adsorbent remains an issue that needs to be addressed immediately. As a raw material, the waste amine oxime resin is easy to obtain and does not require much recultivation like microbial cultivation. The adsorbent prepared from waste amine oxime resin in this article appeared to have a stable structure and could be applied in various environments, thereby reducing Cr toxicity.

Therefore, a novel functionalized mesoporous adsorbent (PPR-Z) was prepared for Cr(VI) adsorption from a waste amidoxime resin. Previous research has often used ion exchange resins as raw materials, while this article supplements the research on using waste amine oxime resin as a carbon source. Furthermore, this article adopts a dual-treatment process involving H_3PO_4 and $ZnCl_2$. Compared with a single-treatment process, the adsorbent prepared using the dual-treatment process exhibits larger adsorption capacity. The prepared adsorbent PPR-Z showed good Cr(VI) selectivity in wastewater. Moreover, PPR-Z has a certain reduction ability, and Cr(VI) can be reduced to Cr(III) during adsorption and desorption. The approach presented in this paper can not only remove Cr(VI) pollution from wastewater but can also effectively solve the problem of waste amidoxime resin treatment, thereby realizing the concept of "treating waste with waste".

2. Experimental

2.1. Materials and reagents

In this experiment, the waste amidoxime resin (PR, Fig. S1) was taken from the Guangxi Branch of the Aluminum Corporation of China. The particle size is 0.2–0.5 mm, and the moisture content is 54.7%. It was used to separate and recover gallium from alkaline Bayer mother liquor and discarded after one month. The discarded amine oxime resin was washed with deionized water three times, then dried in an oven at 50°C for 24 h as raw material. In this study, the following reagents were used: hydrochloric acid (HCl, analytical reagent (AR)), sodium hydroxide (NaOH, AR), phosphoric acid (H_3PO_4, AR), sulfuric acid (H_2SO_4, AR), zinc chloride ($ZnCl_2$, guaranteed reagent (GR)), ferric chloride ($FeCl_3·6H_2O$, AR), potassium dichromate ($K_2Cr_2O_7$, AR), iron nitrate ($Fe(NO_3)_3$, AR), chromium chloride ($CrCl_3$, AR), nickel chloride ($NiCl_2$, AR), sodium chloride (NaCl, AR), ethylenediaminetetraacetic acid (EDTA, AR), potassium permanganate ($KMnO_4$, AR), and ammonium chloride (NH_4Cl, AR). These reagents were purchased from Beijing Sinopharm Group, China.

2.2. Preparation of sorbent

To select the best preparation method, 11 types of adsorption materials were prepared by changing the treatment reagent, pyrolysis temperature, and nitrogen flow speed (see the supplementary material S1 and Table S1 for the preparation process) to investigate their adsorption capacity. The optimal material was found to be PPR-Z, which was prepared as follows: First, waste resin (PR) was washed with deionized water thrice and dried for 24 h in an oven at 50°C. Further, 5 g PR and 50 mL 40vol% H_3PO_4 were added to a 100 mL beaker and stirred at 40°C in a thermostatic water bath at 500

r/min for 4 h. Subsequently, the resin was washed with deionized water thrice and dried in an oven at 50°C for 24 h. Next, $ZnCl_2$ and dried resin with a mass ratio of 1:1 were added to 50 mL water, soaked for 30 min, and then kept in an 80°C oven for curing for 12 h. Further, the resin was placed in a tubular furnace for slow pyrolysis with a heating rate of 3°C/min for 2 h (500°C), and then it was naturally cooled. The pyrolysis process occurred in N_2 atmosphere with a gas flow speed of 0.1 L/min. Finally, after slow pyrolysis, the material was washed with 0.1 mol/L hydrochloric acid (HCl) and deionized water until the pH reached neutral. The sample was then dried at 80°C for 24 h to prepare a new material, PPR-Z.

2.3. Sample characterization

The concentration of Cr(VI) ions in samples before and after adsorption was measured using inductively coupled plasma atomic emission spectrometry (ICP-AES; ICPS-7510, Shimadzu Co, Japan). The synchronous thermal analyzer (SDT650) was used to understand its changes in the heating process under nitrogen atmosphere. The structure of PPR-Z was analyzed using Brooke D8 X-ray diffractometer goniometer (XRD; A24A10). The specific surface area and pore size distribution of PPR-Z were measured using a full-automatic specific surface area analyzer (TriStar II 3020). Morphology observation and energy spectrum analysis were carried out by *in-situ* scanning electron microscope (SEM) nano performance testing and energy spectrum testing system (Sigma 300). The microscopic morphology of PPR-Z was further observed using a 300 kW field emission transmission electron microscope (TEM REI TECNAL G2 F30). The valence state of Cr(VI) ion in solution was identified by ultraviolet−visible−near infrared spectroscopy (UV-3600Plus). The surface charge of PPR-Z was measured using a highly sensitive Zeta potential analyzer (Nanobrook Omni). The chemical structure of the substance was identified by the infrared spectrogram of the sample obtained by Fourier-transform infrared spectroscopy (FTIR; IRTracer-100). Before and after the adsorption, the PPR-Z spectrogram was analyzed to explore the main functional groups and their chemical bonds in the adsorption process. X-ray photoelectron spectroscopy (XPS/INA-X Specs) explored the adsorption mechanism.

3. Results and discussion

3.1. Selection of sorbent

We used phosphoric acid, nitric acid, potassium hydroxide, and $ZnCl_2$ as modifiers to prepare different types of functionalized mesoporous adsorbents, as presented in supplementary information Table S1. Herein, the effect of temperature, atmosphere, and time on the adsorption amount were investigated, as shown in Table 1. The adsorption experiment was performed under the following conditions: 1 g/400 mL, 400 mg/L of Cr(VI) solution, pH = 4, temperature of 303 K, and water bath shaker vibration frequency of 140 r/min. All experiments were set up in three parallel groups to ensure the accuracy of the experimental data. Table 1 shows that the adsorption capacity of the adsorbent prepared using $ZnCl_2$ treatment is better than that of adsorbents prepared by treating with $NiCl_2$, $FeCl_3$, and others. The adsorption capacity of PPR-Z prepared using H_3PO_4 and $ZnCl_2$ was 84.92 mg/g. To better demonstrate the pyrolysis conditions required for preparing PPR-Z, the effects of pyrolysis temperature and nitrogen flow rate on adsorption capacity were studied. Under the same processing conditions, adsorbents PPR-T40 (400°C) and PPR-T60 (600°C) were prepared at different pyrolysis temperatures. Adsorbents PPR-N4 (0.4 L/min) and PPR-N7 (0.7 L/min) were prepared with different nitrogen flow rates while maintaining other conditions same as above. An investigation of the adsorption capacity of the aforementioned adsorbents revealed that their adsorption capacity was less than that of PPR-Z. PPR-Z was the best among all the adsorbents prepared in this experiment. After continuously treated with H_3PO_4 and $ZnCl_2$, the adsorption material (PPR-Z) prepared through slow thermal decomposition exhibits excellent adsorption capacity.

3.2. Material characteristics

3.2.1. Pyrolysis, XRD, and pore size analyses

Thermogravimetric (TG) differential thermal analysis was conducted on untreated waste amidoxime resin (PR) and resin treated with H_3PO_4 and $ZnCl_2$. Fig. 1(a) shows that there are three stages in the weight-loss process. When the temperature increased from 50 to 200°C, the mass loss was about 9.3wt%, mainly caused by the volatilization of residual water molecules in the internal cavities and pores of the resin. The pyrolysis process entered the second stage when the temperature reached 200°C. An exothermic absorption peak appeared on the differential scanning calorimetry (DSC) curve,

Table 1. Adsorption capacity (*Q*) of different adsorbents for Cr(VI)

Number	Name	Temperature / °C	N_2 flow speed / ($L \cdot min^{-1}$)	*Q* / ($mg \cdot g^{-1}$)
1	PPR-Z	500	0.1	84.92
2	PR	500	0.1	9.54
3	PR-4P	500	0.1	50.48
4	PR-5N/$ZnCl_2$ = 1:1	500	0.1	51.12
5	PR/$NiCl_2$	500	0.3	11.32
6	PR + $Fe(NO_3)_3$	800	0.3	27.28
7	PR + 20%KOH	500	0.5	14.64
8	PR-T400	400	0.1	13.88
9	PR-Mn	500	0.3	14.68
10	PR + $FeCl_3$	600	0.3	34.60
11	PR/$ZnCl_2$ = 1:1	500	0.1	68.16
12	PPR-T40	400	0.1	43.37
13	PPR-T60	600	0.1	48.05
14	PPR-N4	500	0.4	48.55
15	PPR-N7	500	0.7	51.76

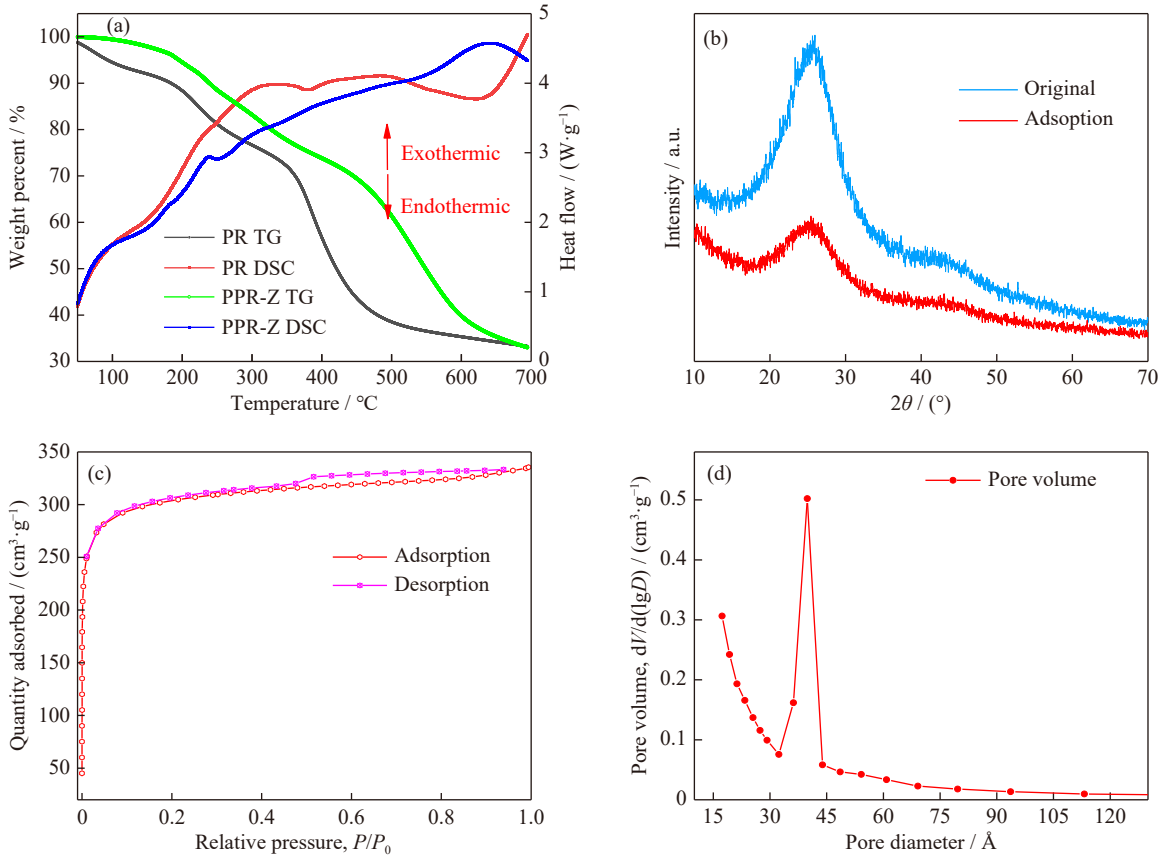

Fig. 1. (a) Thermogravimetric plots of untreated and H_3PO_4 and $ZnCl_2$ treated resins; (b) XRD plots of PPR-Z before and after adsorption; (c) N_2 adsorption–desorption isotherm at standard temperature and pressure; (d) Pore size distribution of PPR-Z.

and its mass loss was attributed to the decomposition of structure on the resin chain and the decomposition of its functional groups [26]. When the temperature continued to rise to the third stage, the mass loss increased by 30wt%, which may be related to the cracking of the styrene chain in the resin and the breaking of C–H on the benzene ring, thus forming an uncertain carbon structure [27]. Fig. 1(a) depicts that the second stage of the resin after treatment with H_3PO_4 and $ZnCl_2$, was extended from 350 to 550°C, and the pyrolysis process shifted from the low-temperature zone to the high-temperature zone. The temperature ranges in the second and third stages were relatively wider. In contrast, the heat release process of PR was relatively concentrated, and more heat was released in a short time, whereas the heat release from the resin treated with H_3PO_4 and $ZnCl_2$ was extended by 50°C, and the heat release process of the DSC curve is smoother. This indicates that the treated resin decomposed more slowly and fully during heating, which is conducive to forming porous structures.

According to the results of a study conducted by Wang *et al.* [28] and Rodrigues *et al.* [29], the pyrolyzed resin would produce a certain type of carbon comprising an aromatic ring structure, edge carbon of graphite sheet layer, and disordered carbon. In addition to using waste resin as a precursor material for the pyrolysis of carbon, a large number of materials can serve as precursors for generating carbon, such as waste tires [30], peanut shells [31], and animal manure [32]. Fig. 1(b) presents the XRD diagram of PPR-Z before and after adsorption. There was a broad diffraction peak between 20° and 30°, corresponding to the peak of amorphous carbon. The peak shape and position of PPR-Z were consistent with that reported by Rodrigues *et al.* [29], indicating that PPR-Z lacked a definite crystal structure, and the resin forms a disordered carbon material during heating and cracking [33].

Fig. 1(c) depicts the N_2 adsorption–desorption isotherm of PPR-Z under relative pressure. The BET data of PPR-Z were consistent with the I-type isotherm model [34] and the H4-type hysteresis loop model [35], respectively. Supplementary information Table S2 shows that the specific surface area of PPR-Z was 1188.58 m^2/g, and the average pore size was 3.3704 nm, indicating many mesopores in PPR-Z after pyrolysis. Fig. 1(d) demonstrates that the pore dimension of PPR-Z was primarily distributed between 3 and 4.5 nm, confirming that PPR-Z contained abundant micropores and mesopores. The H4-type hysteresis loop model shows that the pore structure was irregular and contained narrow fissures [35]. A large specific surface area and abundant micropores and mesopores inside PPR-Z can provide many sites for ion adsorption.

3.2.2. Morphological and structural analysis

Fig. 2 depicts the characterization of PPR-Z using SEM and energy dispersive spectrometer (EDS). The PPR-Z prepared by pyrolysis has an irregular sheet structure, exhibiting numerous pore structures on its surface. Fig. 2(b) and (c) shows that the PPR-Z surface is uneven. On magnifying to 100 nm, many slit pore structures are revealed to be distrib-

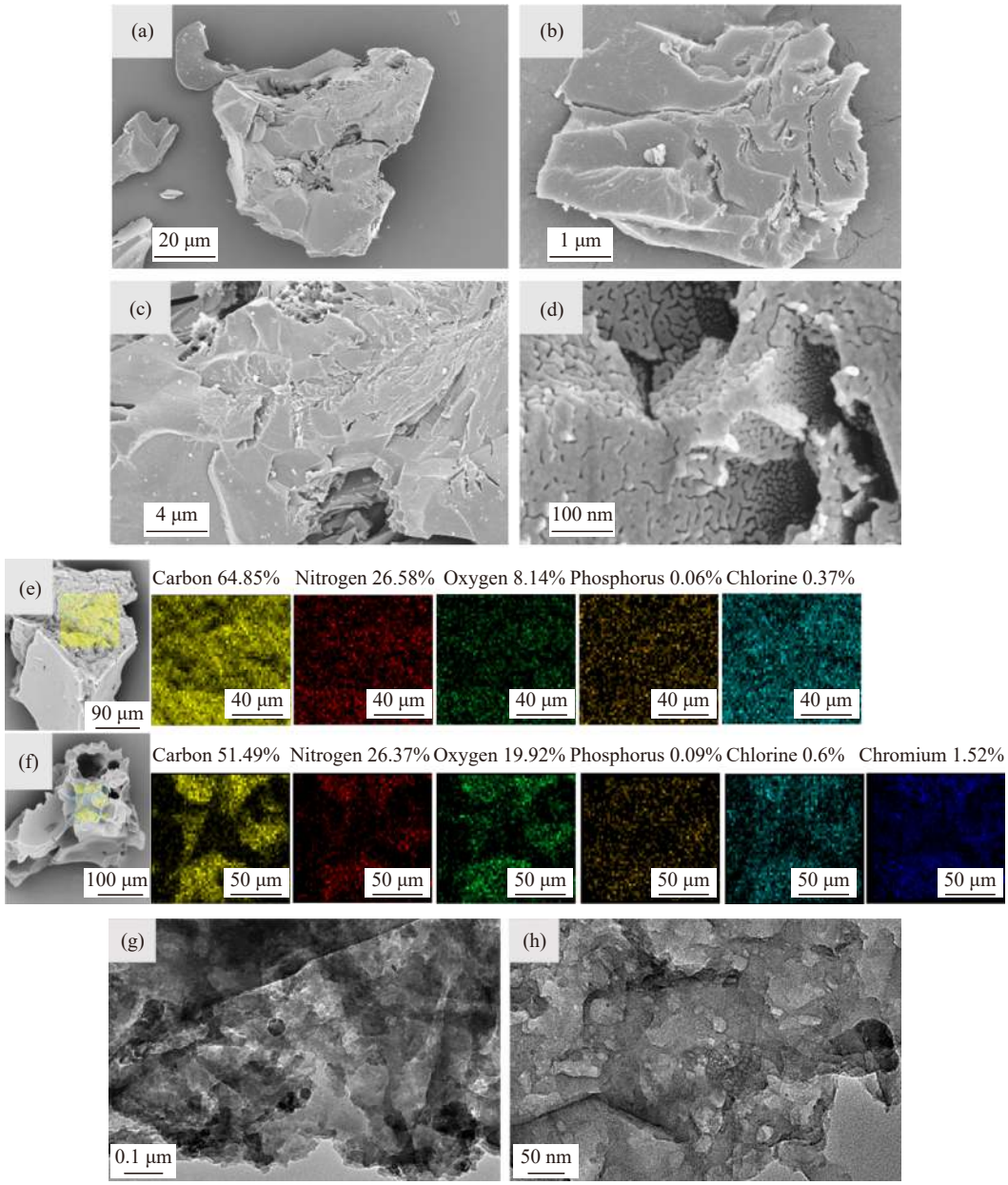

Fig. 2. (a–d) SEM images of PPR-Z; EDS images of PPR-Z (e) before and (f) after adsorption; (g–h) TEM morphological analysis of PPR-Z.

uted on the smooth PPR-Z surface, as shown in Fig. 2(d). This proves that the pore structure of PPR-Z is irregular and belongs to narrow fissure holes and distribution of surface and interior of PPR-Z, increasing the specific surface area of the material. Fig. 2(e) depicts that PPR-Z mainly comprises C, N, O, and P. After adsorption, PPR-Z adsorbs Cr(VI), as shown in supplementary information Table S3.

To further understand the micropore structure on the surface of the PPR-Z sample, its morphology was analyzed using a TEM, as shown in Fig. 2(g) and (h). The sample contains numerous pore structures on its surface and inside, and the distribution distance between the pores is very close. the change in the light field can reveal a part of the pore structure, but there are only a few regular round pores, indicating that there are predominantly irregular slit pores. The uneven distribution of bright and dark fields at a magnification of 50 nm indicates that the sample surface and its internal pore structures are irregular.

Therefore, BET, SEM, and TEM have confirmed that PPR-Z has a very dense pore structure, which turns into an irregular sheet material at the macro level. At the micro level, the surface of the material looks smooth, with some mesopores and macropores. Many fissure pores on the surface and inside of the material provide favorable conditions for adsorption.

3.3. Cr(VI) adsorption experiment

3.3.1. Influence of pH and ion selectivity

One of the major features affecting the adsorption efficacy is acidity. The acidity of the aqueous phase will influence the surface charge of the adsorbent, degree of ionization, and surface metal binding sites. The effect of initial pH on the adsorption capacity (Cr) of three adsorbents (PR, PR-4P, and PPR-Z) is presented in Fig. 3. With an adsorption capacity of

98.21 mg/g at pH = 2, PPR-Z exhibited the highest adsorption capacity among the three. When pH was gradually increased to 9, the adsorption capacity decreased to 26.64 mg/g. Moreover, PPR-Z showed a better adsorption capacity for Cr(VI) under acidic conditions. This may be because the surface positive charge of PPR-Z changed with the pH of the solution, resulting in a competition between OH^- and Cr. As pH increased, OH^- hindered the attraction of PPR-Z for Cr(VI), thereby reducing its adsorption capacity [36]. As shown in Fig. 3(a), with an increase in the pH, the adsorption capacity of Cr(VI) by PR increased. The main reason for this is that the amine oxime resin (PR) relied on amino ($–NH_2$) and oxime group (–C=N–OH) to form stable coordination complexes with metal ions. When the acidity was high, $–NH_2$ was protonated to form $–NH_3^+$ [37]. Conversely, when pH increased, deprotonation of $–NH_3^+$ caused the generation of $–NH_2$. Hence, stable complexes could be formed with Cr ions through the combined action of amino and oxime groups. Due to the presence of a small portion of amine oxime groups in waste amine oxime resin, the PR adsorption capacity remained unchanged as the pH increased. Therefore, the adsorption capacity of Cr(VI) by PR was very low, and its maximum adsorption capacity was only 11.7 mg/g. The adsorption capacity of PR-4P for Cr(VI) was 80.84 mg/g at pH = 1, which decreased with increasing pH.

Fig. 3(b) shows that PPR-Z can selectively adsorb Cr at a pH range of 1–3. When pH = 2.5, the adsorption capacity of PPR-Z for Cr(VI) is 97.37 mg/g, and the adsorption capacity for Al, Ca, Ni, and Zn is relatively low. PPR-Z has a low adsorption capacity for Cu, which gradually increases with pH. When pH = 3, the adsorption capacity for Cu reaches 24.82 mg/g. Fig. 3(c) presents the calculated results of separation coefficient (SF) [38] under different pH conditions; when pH = 2, $SF_{Cr/Al}$ = 24.32, $SF_{Cr/Ca}$ = 20.17, $SF_{Cr/Ni}$ = 68.43, $SF_{Cr/Zn}$ = 36.98, and $SF_{Cr/Cu}$ = 10.65. The adsorption order of PPR-Z for ions obtained in electroplating waste liquid is Cr > Cu > Ca > Al > Zn > Ni. The adsorbent PPR-Z exhibits selectivity for ions in electroplating wastewater, and it is a good material for treating Cr(VI) in electroplating wastewater [39].

Various cations and anions exist in actual electroplating wastewater solutions [38,40]. The specific pH, ion types, and solubility are shown in supplementary information Table S4. The adsorption capacity of PPR-Z for cations in actual chromium-containing wastewater under different pH conditions was carried out to demonstrate the adsorption characteristic of PPR-Z. As shown in Fig. 3(d), at pH = 2, the adsorption capacity of PPR-Z for Cr reached 97.05 mg/g, and the adsorption capacity for other cations was very low. Moreover, as pH rose, iron ions in the solution began to precipitate. The co-precipitation of iron ions [41] decreased the concentration

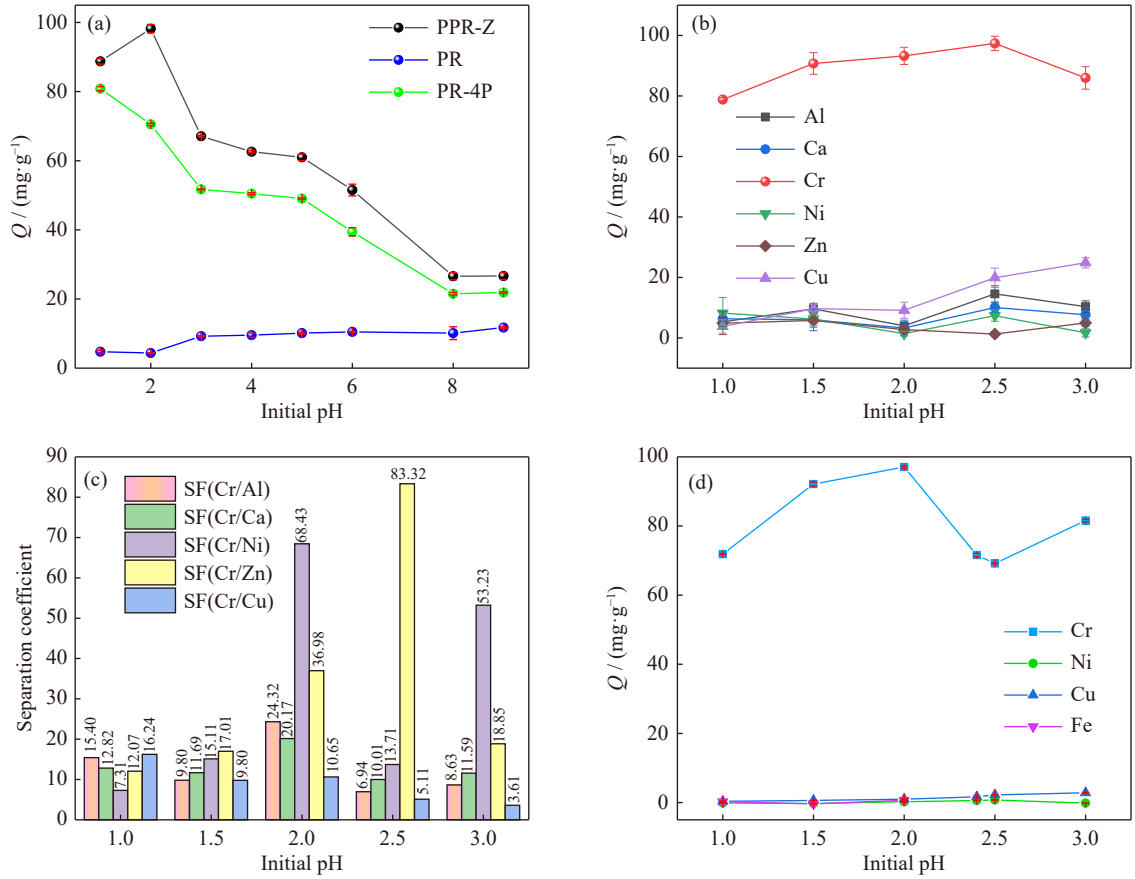

Fig. 3. (a) Effect of initial pH on the adsorption capacity of Cr(VI) (adsorbent *m* = 50 mg, *V* = 20.0 mL, *T* = 303 K, C_0(Cr) = 400 mg/L, time = 6 h); (b) Selectivity of PPR-Z for different ions at different pH (adsorbent *m* = 50 mg, metal ion: 300 mg/L, *T* = 303 K, *V* = 40.0 mL, time = 12 h); (c) Separation coefficient of PPR-Z for Cr at pH of 1–3 in mixed systems; (d) Simulation results for the adsorption capacity of different ions in a real solution.

of Cr(VI) ions in the solution, which was the main reason for the increased adsorption capacity of Cr at pH = 3. It can be concluded that PPR-Z has good selectivity for ions in actual electroplating wastewater, providing a solution for PPR-Z to achieve the treatment and recovery of Cr in actual wastewater.

3.3.2. Adsorption kinetics

Fig. 4(a) depicts the effect of time on the adsorption capacity of PPR-Z for Cr(VI). Due to the presence of numerous pore structures and adsorption sites at the early stage of adsorption, the adsorption efficiency of PPR-Z for Cr(VI) is high. After 2 h of adsorption, the adsorption capacity reached 92% of the equilibrium adsorption capacity, and then the adsorption efficiency decreased with time. It took 8 h to reach the adsorption equilibrium for Cr(VI). When the temperature increased from 293 to 313 K, the time to reach adsorption equilibrium was reduced from 8 to 4 h. An increase in the temperature can also reduce the time required to reach adsorption equilibrium, whereas the maximum adsorption capacity only increased from 138.25 to 143.15 mg/g with increasing temperature, indicating that the change in temperature has little effect on the adsorption capacity at equilibrium. The pseudo-first-order (PFO), pseudo-second-order (PSO) [42], and Weber–Morris (W-M) intraparticle diffusion mod-

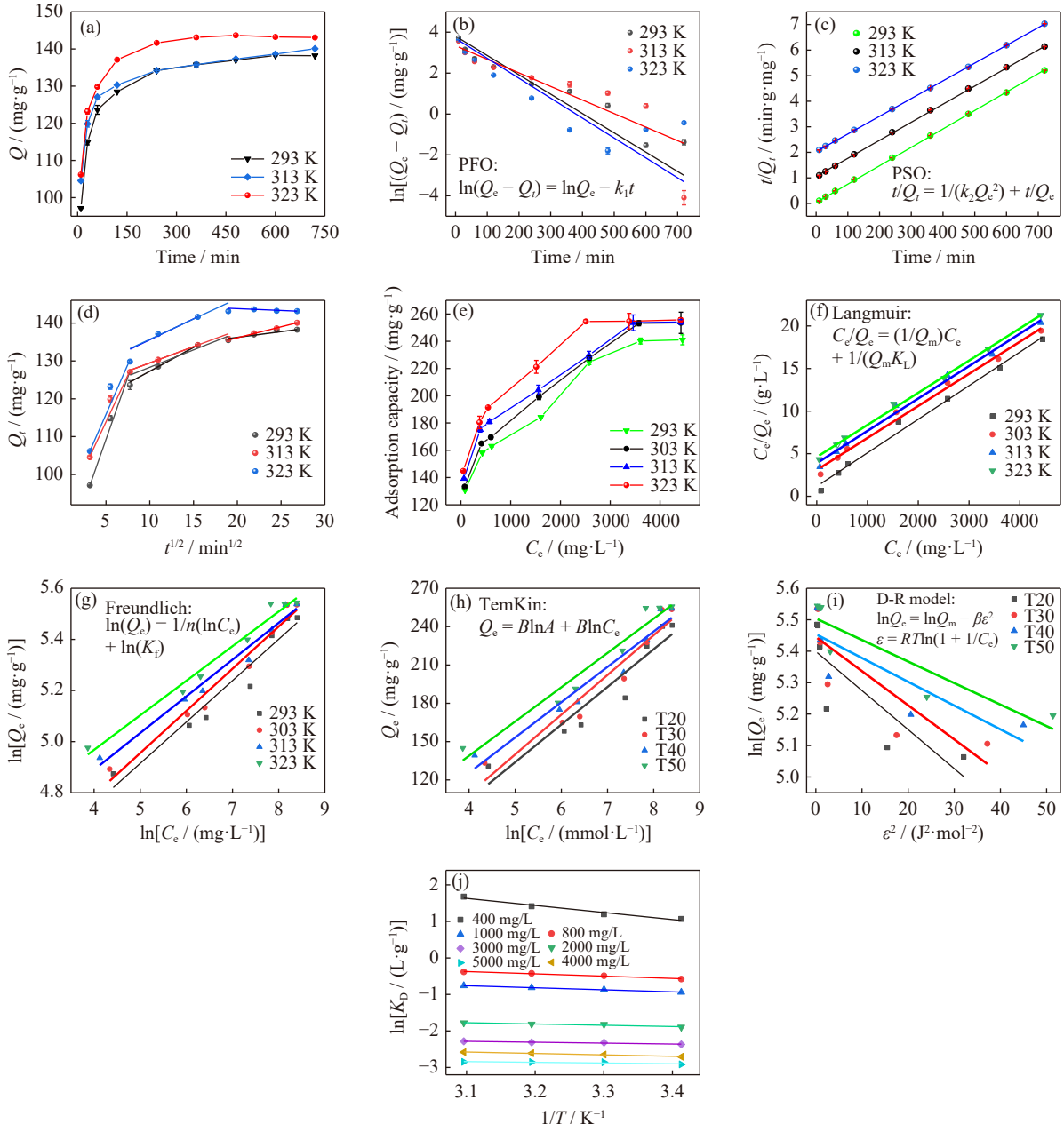

Fig. 4. (a) Adsorption capacity vs. time (adsorbent *m* = 50 mg, *V* = 20.0 mL, pH = 2, and C_0 = 400 mg/L), (b) Pseudo-primary model fit, (c) pseudo-secondary model fit, and (d) Weber–Morris intraparticle diffusion model; (e) Variations in Cr(VI) adsorption amount with Cr(VI) concentration (adsorbent *m* = 50 mg, *V* = 20.0 mL, pH = 2, and Time = 8 h); (f) Langmuir isothermal model fit, (g) Freundlich isothermal model fit, (h) Temkin isothermal model fit, (i) D-R isothermal model fit, and (j) thermodynamic fit for different Cr(VI) concentrations.

el were used to fit the adsorption kinetic data of Cr(VI) ions (Fig. 4(b), (c), and (d)). By comparing the fitted parameters in the supplementary material Table S5, it was determined that the adsorption of Cr(VI) by PPR-Z follows the PSO kinetic model, indicating that the Cr(VI) adsorption by PPR-Z was an adsorption process controlled primarily by the chemical adsorption mechanism [43–44].

As shown in Fig. 4(d) and supplementary material Table S5, the adsorption process of Cr(VI) by PPR-Z is divided into three stages. The slope is the largest at the initial stage, and the adsorption capacity increases significantly. The removal rate of Cr(VI) ions is the highest. Due to the large specific surface area and microporous, the diffusion resistance of Cr ions is small. Surface adsorption and microporous surface adsorption were dominant at the first stage. In the second stage, the slope became smaller. Cr(VI) ions diffused into PPR-Z through mesoporous and were adsorbed by adsorption sites on the interior surface. Finally, due to the concentration of Cr(VI) in the solution decreasing rapidly and ultra-fine pore diffusion, the diffusion resistance increased, and the adsorption rate decreased at low temperatures. As the temperature increased to 323 K, diffusion was enhanced, and the adsorption gradually reached equilibrium [45]. The linear equation fitted in the three stages does not pass through the origin, which indicates that the external diffusion control of particles is also the rate control step of the adsorption process [46].

3.3.3. Adsorption isotherms and thermodynamics

Isothermal adsorption lines are often used as an important reference for evaluating the capacity of various adsorbents in practical work. They are the necessary data required to describe the interaction between adsorbents and ions. The saturated adsorption capacity of PPR-Z for various Cr(VI) concentrations (400–5000 mg/L) is shown in Fig. 4(e). The adsorption capacity of PPR-Z for Cr(VI) increased with an increase in the initial concentration of Cr(VI). When the initial concentration was 4000 mg/L, the adsorption capacity reached saturation. As the temperature increased, the adsorption capacity slightly increased. At 323 K, the maximum saturated adsorption capacity of PPR-Z for Cr(VI) was 255.68 mg/g. To objectively evaluate the adsorption capacity of PPR-Z, we compared the adsorption capacity of PPR-Z with those of other carbon-based adsorption materials, as shown in Table 2. The adsorbent AC-KOH-750 has a large specific surface area and strong adsorption capacity reaching 370.37 mg/g, due to its modification of pore structure with KOH. The adsorption capacity of CeO_2-modified adsorbent KSAC-CeO_2 for Cr(VI) was only 14.00 mg/g. Among them, we have selected several representative carbon-based adsorbents, namely, magnetic carbon composites (M-AC), porous Biochar (ZVI@TBC), carbon nanocomposites (C-DE@S), and carbon nanotubes (MU-CNTs/Fe-700). The adsorption capacity of PPR-Z is then compared with those of these materials to reflect its higher adsorption capacity.

Langmuir, Freundlich, and Temkin isotherm models were used to fit the adsorption data (Fig. 4(f), (g), and (h)). Supplementary material Tables S6 and S7 show that Langmuir's R^2 is 0.99, Freundlich's R^2 is 0.95, and Temkin's R^2 is only 0.89 at 293 K, indicating that the Langmuir isotherm model fits well. Cr(VI) was uniformly adsorbed on PPR-Z in the form of a single molecular layer, which may be related to the high specific surface area and rich pore structure of PPR-Z [55]. By fitting the data with the Dubin Radushkevich (D-R) isothermal adsorption model, the R^2 at 323 K was only 0.7818, but the change in free energy during the adsorption process can be found through fitting. According to supplementary material Table S7, when the temperature is higher than 303 K and the energy is higher than 8 kJ·mol^{-1}, the process is dominated by chemical adsorption, confirming the conclusion of adsorption kinetics fitting. Therefore, the adsorption of ions on the adsorbent was uniform, indicating that the single molecule chemistry adsorption mechanism was responsible [56].

Table 2. Amount of Cr(VI) adsorbed by different carbon-based adsorbents

Adsorbents	Q / (mg·g^{-1})	Reference
PPR-Z	255.68	This work
KSAC-CeO_2	14.00	[10]
SLACM	227.7	[47]
AC-NH_3-900	95.60	[48]
AC-KOH-750	370.37	[48]
ACSs	230.15	[49]
chitosan	82.78	[50]
NTP	6.48	[45]
M-AC	58.39	[51]
ZVI@TBC	186.2	[52]
C-DE@S	142.827	[53]
MU-CNTs/Fe-700	23.7	[54]

The thermodynamics of the adsorption process is a crucial factor affecting the adsorption process. The thermodynamic parameters of the system are calculated using supplementary material S2 Eqs. (S12), (S13), and (S14). As shown in Fig. 4(j), to obtain Gibbs free energy change ΔG, enthalpy (ΔH), and entropy (ΔS) are first obtained from slope and intercept. Supplementary material Table S8 shows that the entropy (ΔS) decreases from a positive to a negative value with increasing concentration of initial ion, indicating that an increase in the ion concentration decreases the vacancy resistance during adsorption. This is conducive to adsorption; additionally, enthalpy (ΔH) also decreases with a change in the ion concentration, implying that the adsorption of Cr(VI) by PPR-Z is a rather complex process [57]. Enthalpy (ΔH) is positive for Cr(VI) adsorption by PPR-Z, indicating that this process is endothermic. At the same concentration, the value of ΔG decreases with an increase in the temperature, suggesting that the reaction is spontaneous; moreover, an increase in the temperature promotes adsorption [58].

3.4. Chemical reduction and cyclic performance

3.4.1. Chemical reduction

The desorption rate and reuse cycle of the adsorbent are important factors affecting regeneration. Fig. 5(a) depicts the influence of desorption type and concentration of desorption agent on the desorption rate of Cr. As shown in Fig. 5(a),

5 mol/L sulfuric acid (H_2SO_4) exhibits the best desorption for Cr. Therefore, sulfuric acid (H_2SO_4) is used as the desorption agent. The concentration of the desorption agent, the amount of the desorption agent, and the desorption temperature and time were investigated, as shown in Fig. 5(b) and (c). Fig. 5(b) depicts that the desorption efficiency of Cr(VI) increased with an increase in the H_2SO_4 concentration, while Cr(VI) desorption rate reached 81% with the addition of 5 mol/L sulfuric acid. When the solution volume gradually increased from 20 to 120 mL (Fig. 5(b)), there was little change in the Cr(VI) desorption rate. Moreover, temperature exerted a significant influence on the desorption rate (Fig. 5(c)). When the temperature increased from 283 to 323 K, the time to reach the desorption equilibrium was reduced from 540 to 360 min, and the desorption rate increased from 32.18% to 74.23%, indicating that an increase in the temperature could not only reduce the time required for desorption to reach equilibrium, but also improved the desorption rate. The desorption experiment revealed that the desorption rate for 5 mol/L sulfuric acid reached 81.47% at

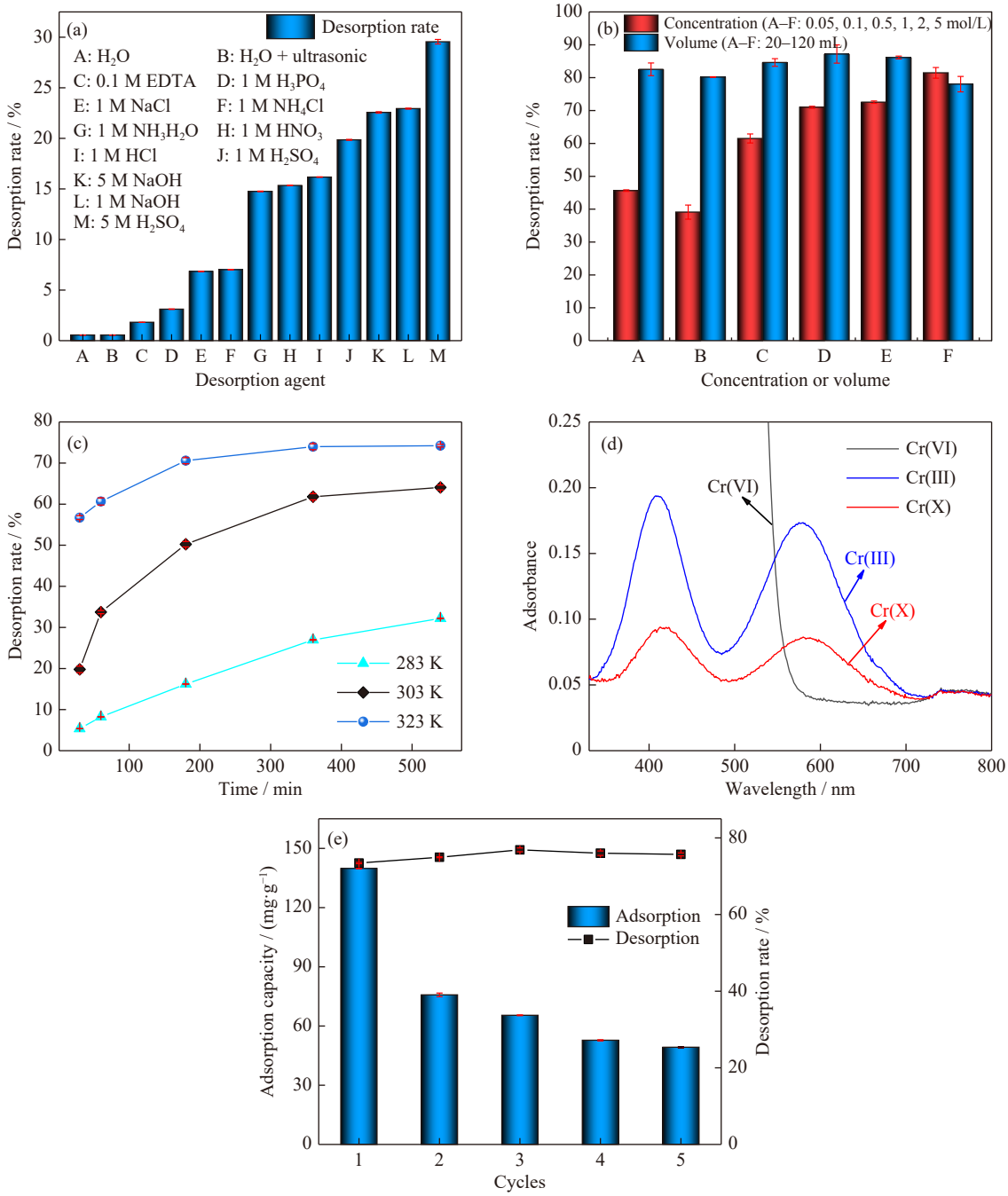

Fig. 5. (a) Desorption rates of different desorbents (adsorbent *m* = 50 mg, *V* = 20.0 mL, *T* = 303 K, and time = 2 h); (b) Desorption rates for Cr(VI) at different Molar concentration and volumes of desorbents (adsorbent *m* = 50 mg, *V* = 40.0 mL, *T* = 303 K, and time = 16 h); (c) Desorption rates for Cr(VI) at different times and temperatures of desorbents (adsorbent *m* = 50 mg, *V* = 40.0 mL); (d) UV spectra of Cr(VI), Cr(III), and Cr(X) solutions after desorption; (e) Experiment for measuring the cyclic performance of PPR-Z.

323 K.

To prove the reduction effect of PPR-Z on Cr(VI) during desorption and understand the valence state of Cr ions after desorption, $K_2Cr_2O_7$ and $CrCl_3$ solutions with a concentration of 500 mg/L in 5 mol/L H_2SO_4 were prepared. The solution with Cr(X) is the desorption solution of PPR-Z. The most common valence states of Cr are Cr(VI) and Cr(III), while Cr(III) is a very stable valence state and exists in different forms at different pH values [14,55]. When pH < 3.9, Cr(III) exists in the form of water-soluble Cr^{3+} cation, and the amount of Cr^{3+} decreases gradually with the increase of pH to 5. $Cr(OH)^{2+}$ is formed when pH > 5, and when pH > 6, a precipitate of $Cr(OH)_3$ is formed, which exists in different forms with different colors at different pH [55]. The solution was further analyzed using ultraviolet (UV) spectroscopy to determine the valence form of Cr(X), as shown in Fig. 5(d). Because Cr(VI) ions are in their highest valence state, there is no obvious absorption peak. Cr(III) exhibits two absorption peaks at wavelengths of 410 and 580 nm [59]. Moreover, the wavelength of the absorption peak of Cr(X) matches that of Cr(III), indicating that Cr in the desorption solution Cr(X) existed as Cr(III). PPR-Z is compared with conductive polyaniline-modified anaerobic granular sludge (AGS) prepared by Chai *et al.* [60]. Both adsorbents reduce Cr(VI) to Cr(III). AGS is used for the reduction of Cr(VI) to Cr(III) and adsorption the Cr(III). However, a part of Cr(VI) is reduced to Cr(III) during the Cr(VI) adsorption by PPR-Z, and the rest of Cr(VI) is reduced to Cr(III) during desorption. Therefore, the toxicity of Cr(VI) is reduced during adsorption and desorption.

Acidic conditions can effectively provide H^+ to reduce Cr(VI) at pH = 2. Therefore, it was assumed that the following reactions occurred in process [61]:

$$Cr_2O_7^{2-} + 14H^+ + 6e^- \leftrightarrow 2Cr^{3+} + 7H_2O.$$

The XPS spectra presented demonstrate this phenomenon. The narrow spectrum of Cr adsorbed in PPR-Z shows peak intensities of Cr(III) at 588.25 and 579.10 eV, indicating that PPR-Z has indeed reduced some Cr(VI) to Cr(III) in the presence of hydrogen ions after adsorption. A large amount of H^+ was consumed during the reduction of Cr(VI). When 5 mol/L H_2SO_4 was used as a desorption agent to desorb Cr ions, Cr(VI) adsorbed on PPR-Z was reduced to Cr(III). Because PPR-Z was positively charged, the reduced Cr(III) was also positively charged, and under electrostatic action, Cr(III) was discharged from the pore structures of PPR-Z.

3.4.2. Cyclic performance

Fig. 5(e) shows that under the same adsorption and desorption conditions, after five cycles, the adsorption capacity of PPR-Z gradually decreased to one-third of its original value, indicating that PPR-Z has a certain cycling value. On the one hand, due to the incomplete desorption of Cr(VI), it will occupy the active site of the adsorbent. On the other hand, the reduction in its adsorption capacity may be a result of the reduction of Cr(VI) to Cr(III) during the desorption process, which destroys the original structure of PPR-Z [62], thereby reducing the adsorption capacity of PPR-Z.

3.5. Adsorption mechanism

Zeta potential, FT-IR, and XPS techniques were used to explore the adsorption mechanism. As shown in Fig. 6(a), PPR-Z has the same charged property as ZnNiCr-layered double hydroxides [63]. The potential of adsorbent PPR-Z is positive before pH reached 10.15, and the positive potential strength is high, indicating that adsorbent PPR-Z itself is positively charged, whereas Cr(VI) exists as negative ions in the solution ($Cr_2O_7^{2-}$). Therefore, ZnNiCr-layered double hydroxides and PPR-Z can interact electrostatically with Cr(VI) ions [64]. Through charge attraction, Cr(VI) in solution can enter inside the PPR-Z, accelerating the combination of ions and active sites, which is conducive to improving the adsorption efficiency.

The infrared spectrogram before and after the adsorption in Fig. 6(b) reveals the presence of –OH, $–CH_2$, –C=O, –C–O, and –CH in PPR-Z adsorbent at peak positions 3415, 2924, 1578, 1185, and 755 cm^{-1}, respectively. These are functional groups that can exist after the pyrolysis of waste amine oxime resin. Several consecutive absorption peaks at 907 and 750 cm^{-1} correspond to the stretching vibration of –CH in the benzene ring [1]. The absorption peak of –C=O shifts from 1578 to 1593 cm^{-1} after adsorption, and the –C=O in PPR-Z also exhibits a significant shift, indicating that the functional group –C=O interacts with Cr(VI) during the adsorption process. The desorption curve shows that when Cr(VI) is eluted from PPR-Z, the –C=O absorption peak returns to the wavelength 1578 cm^{-1} [58].

PPR-Z was analyzed using XPS spectra before and after adsorption. According to the full spectrum of PPR-Z before and after adsorption in Fig. 6(c), the characteristic peaks of C 1s, N 1s, and O 1s are at 280, 400, and 530 eV, respectively, and the characteristic peaks of Cr appear at 580 eV for the adsorbed PPR-Z [65]. This indicates that Cr(VI) was adsorbed onto PPR-Z. Fig. 6(d) depicts that Cr adsorbed on PPR-Z exhibited two characteristic double peaks, one high and one low. After the adsorption of Cr on PPR-Z, peaks corresponding to Cr(VI) (577.10 and 586.70 eV) [35] and Cr(III) (579.10 and 588.25 eV) [66–67] appeared. Simultaneously, the intensity of the Cr(VI) bimodal is larger than that of Cr(III), indicating that Cr(VI) remained in its main valence state during the adsorption process. Due to the insufficient supply of H^+ in the solution during adsorption, only a portion of Cr(VI) was reduced to Cr(III), consistent with the results of the UV spectroscopic experiments.

Combined with infrared data, Fig. 6(b), (e), and (f) confirms that –C=O plays a major role in adsorption. In the narrow spectrum of oxygen, peaks at 531.15, 532.30, and 533.55 eV correspond to –OH, –C–O, and –C=O, respectively. The binding energy of –C=O shifts from 533.55 to 532.85 eV after adsorption, while that of –C–O in the carbon narrow spectrum only shifts from 289.10 to 288.85 eV. Thus, the binding energy shift (0.25 eV) is much smaller than the binding energy shift (0.7 eV) in the oxygen narrow spectrum, indicating that –C=O changed during the adsorption process and chelated with Cr(VI) at the position of oxygen, making

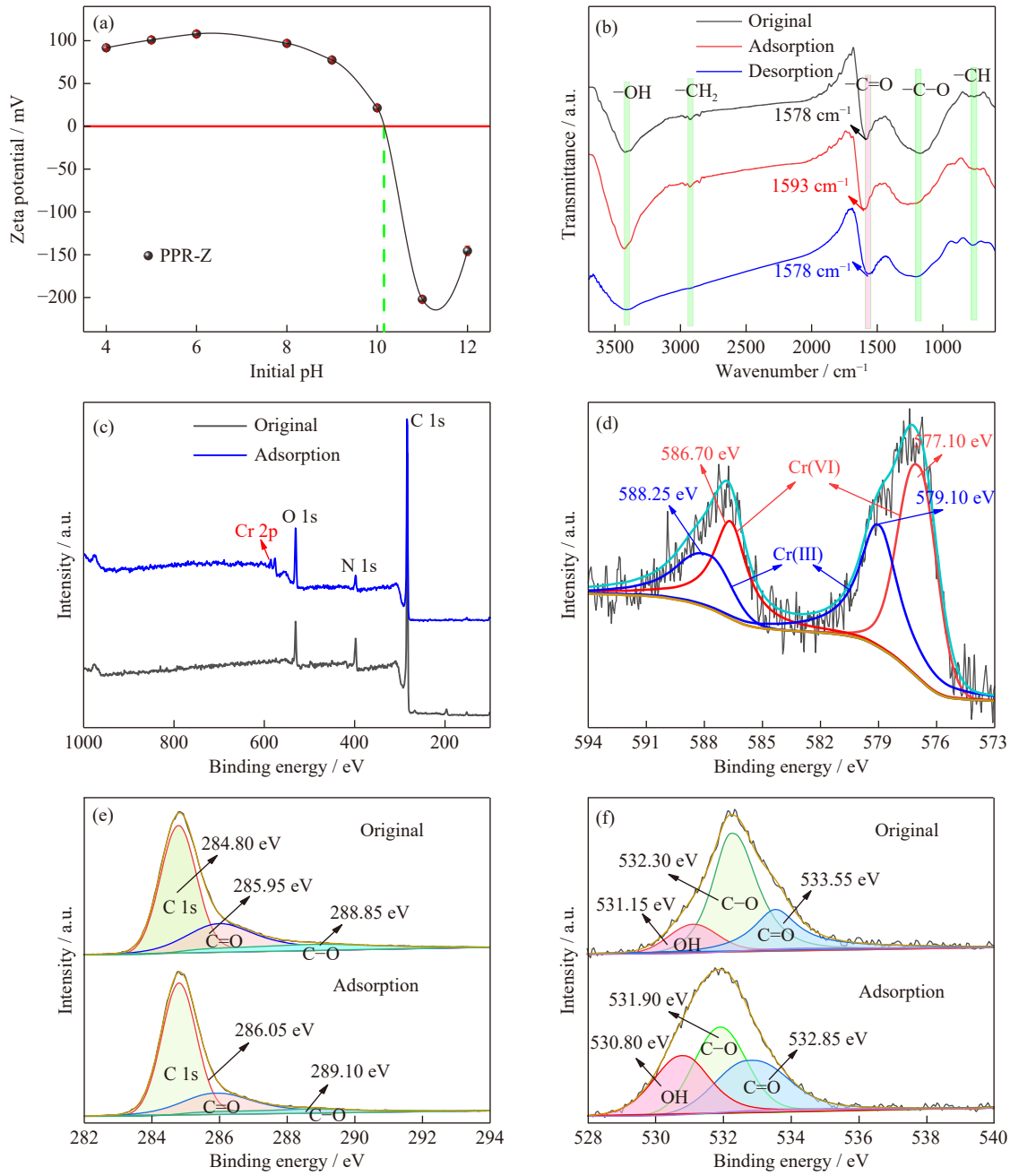

Fig. 6. (a) Zeta potential of PPR-Z at different pH; (b) FT-IR spectra of PPR-Z before and after adsorption; (c) XPS full spectrum of PPR-Z before and after adsorption; (d) XPS Cr(VI) narrow spectrum of PPR-Z after adsorption; (e) XPS carbon narrow spectrum of PPR-Z before and after adsorption; (f) XPS oxygen narrow spectrum of PPR-Z before and after adsorption.

its binding energy change significantly (0.7 eV) [35].

4. Conclusions

The functionalized mesoporous adsorbent PPR-Z was prepared with waste amine oxime resin as raw material and treated with H_3PO_4 and $ZnCl_2$ through slow thermal decomposition. The maximum adsorption capacity of PPR-Z was 255.68 mg/g at pH = 2, T = 323 K, and t = 8 h. The PSO kinetic model and Langmuir isotherm agreed with the experimental data, proving that the adsorption of Cr(VI) by PPR-Z is a single-layer adsorption dominated by chemical adsorption. The maximum desorption rate of 5 mol/L sulfuric acid (H_2SO_4) for Cr(VI) reached 81% at 50°C and 6 h. Estimation of SF value using an ion selectivity experiment revealed that PPR-Z exhibited adsorption selectivity for Cr(VI) in electroplating wastewater.

PPR-Z presents an irregular block shape, and the SEM and TEM analyses implied that the pore structure of PPR-Z is distributed on its surface and inside. The BET analysis shows that PPR-Z has a large specific surface area, with an average pore size of 3.3704 nm and a specific surface area of 1188.58 m^2/g. The internal pore structure was characterized using uneven fissure holes.

According to zeta potential analysis, the positive charge of PPR-Z itself is conducive to the adsorption of Cr(VI). Before and after the adsorption, the FT-IR spectra showed that C=O and Cr have chelated during adsorption. The binding energy

of –C=O during the adsorption process obtained by combining FTIR with XPS suggests that it may have interacted with Cr(VI) at the position of oxygen. According to the UV analyses, PPR-Z can reduce Cr(VI) to Cr(III). PPR-Z prepared from waste amidoxime resin is an effective and low-cost environmental protection material for adsorbing Cr(VI) from electroplating waste liquid. Simultaneously, its excellent physical and chemical properties can be further optimized to improve its adsorption and desorption performance. Moreover, it can be a reference for using mesoporous adsorbent materials to extract other metal ions.

Acknowledgements

This research was supported by the National Natural Science Foundation of China (No. 52364022), the Natural Science Foundation of Guangxi Province, China (Nos. 2023JJA160192 and 2021GXNSFAA220096), the Guangxi Science and Technology Major Project, China (No. AA23073018), and the Guangxi Chongzuo Science and Technology Plan, China (No. 2023ZY00503).

Conflict of Interest

The authors declare that they have no known competing financial interests or personal relationships that could have appeared to influence the work reported in this paper.

Supplementary Information

The online version contains supplementary material available at https://doi.org/10.1007/s12613-023-2737-z.

Nomenclature

m	Mass
C_0	Initial concentration
C_e	Equilibrium concentration of Cr(VI) after adsorption
t	Time
k_1	Quasi-first order kinetics rate constant
k_2	Quasi-second order kinetics rate constant
K_f	Freundlich adsorption isotherm equation constant
K_D	Dispersion coefficient
K_L	Langmuir adsorption isotherm equation constant
β	Constant related to adsorption energy
R	Ideal gas constant
V	Volume
T	Temperature
Q_e	Balanced adsorption capacity
Q_t	Adsorption capacity at t time
Q_m	Saturated adsorption capacity
ε	Polanyi potential

References

[1] C.L. He, Y. Liu, C.H. Zheng, *et al*., Utilization of waste amine-oxime (WAO) resin to generate carbon by microwave and its removal of Pb(II) in water, *Toxics*, 10(2022), No. 9, art. No. 489.

[2] C.H. Zheng, C.L. He, Y.J. Yang, T. Fujita, G.F. Wang, and W.C. Yang, Characterization of waste amidoxime chelating resin and its reutilization performance in adsorption of Pb(II), Cu(II), Cd(II) and Zn(II) ions, *Metals*, 12(2022), No. 1, art. No. 149.

[3] Z. Laili, M.S. Yasir, and M.A. Wahab, Solidification of radioactive waste resins using cement mixed with organic material, *AIP Conf. Proc.*, 1659(2015), art. No. 050006.

[4] S. Keck, O. Liske, K. Seidler, *et al*., Synthesis of a liquid lignin-based methacrylate resin and its application in 3D printing without any reactive diluents, *Biomacromolecules*, 24(2023), No. 4, p. 1751.

[5] S.H. Yang, H. Fang, H. Li, *et al*., Synthesis of tung oil-based vinyl ester resin and its application for anti-corrosion coatings, *Prog. Org. Coat.*, 170(2022), art. No. 106967.

[6] J.S. Shon, H.K. Lee, T.J. Kim, J.W. Choi, W.Y. Yoon, and S.B. Ahn, Evaluation of utility of the cement solidification process of waste ion exchange resin, *Toxics*, 10(2022), No. 3, art. No. 120.

[7] U.K. Chun, K. Choi, K.H. Yang, J.K. Park, and M.J. Song, Waste minimization pretreatment via pyrolysis and oxidative pyroylsis of organic ion exchange resin, *Waste Manage.*, 18(1998), No. 3, p. 183.

[8] X.B. Zhang, M. Liu, and X. Gao, The co-combustion and pollutant emission characteristics of the three kinds of waste ion exchange resins and coal, *Int. J. Chem. React. Eng.*, 18(2020), No. 8, art. No. 20200053.

[9] X.J. Peng, W. Zeng, H.H. Miao, S.J. Lu, and S.S. Li, A novel carbon adsorbent derived from iron-poisoned waste resin for phosphate removal from wastewater: Performance and mechanism, *Process. Saf. Environ. Prot.*, 168(2022), p. 324.

[10] Y. Yang, J.C. Qian, Z. Yu, L. Shi, and X. Meng, Preparation of hierarchically porous carbon spheres derived from waste resins and its application in water purification, *J. Porous Mater.*, 26(2019), No. 1, p. 163.

[11] M. Wojtaszek and R. Wasielewski, The use of waste ion exchange resins as components of the coal charge for the production of metallurgical coke, *Fuel*, 286(2021), art. No. 119249.

[12] C. Campillo-Cora, L. Rodríguez-González, M. Arias-Estévez, D. Fernández-Calviño, and D. Soto-Gómez, Influence of physicochemical properties and parent material on chromium fractionation in soils, *Processes*, 9(2021), No. 6, art. No. 1073.

[13] R.N. Bharagava and S. Mishra, Hexavalent chromium reduction potential of Cellulosimicrobium sp. isolated from common effluent treatment plant of tannery industries, *Ecotoxicol. Environ. Saf.*, 147(2018), p. 102.

[14] M. Shahid, S. Shamshad, M. Rafiq, *et al*., Chromium speciation, bioavailability, uptake, toxicity and detoxification in soil-plant system: A review, *Chemosphere*, 178(2017), p. 513.

[15] L.Q. Liang, J.H. Wang, and Y.X. Zhang, Magnetic mesoporous carbon hollow microspheres adsorbents for the efficient removal of Cr(III) and Cr(III)-EDTA in high salinity water, *Microporous Mesoporous Mater.*, 347(2023), art. No. 112344.

[16] Q. Sun, C.L. Wang, L.X. Zhang, and Y.Z. Yang, Thiourea crosslinked-amino modified graphene nanoflakes as an effective adsorbent to confine Cr(VI) via multiple combination mechanisms, *J. Cleaner Prod.*, 374(2022), art. No. 134030.

[17] A. Zhitkovich, Chromium in drinking water: Sources, metabolism, and cancer risks, *Chem. Res. Toxicol.*, 24(2011), No. 10, p. 1617.

[18] S. Alharthi, S.A. Alharthy, E.S.A. Manaa, M.O.A. El-Magied, and W.M. Salem, High adsorption performance of Cr(VI) ions from the electroplating waste solution using surface-modified porous poly 2-((methacryloxy)methyl)oxirane polymers, *Z. Anorg. Allg. Chem.*, 648(2022), No. 19, art. No. e202100327.

[19] H. Peng and J. Guo, Removal of chromium from wastewater by membrane filtration, chemical precipitation, ion exchange, adsorption electrocoagulation, electrochemical reduction, electrodialysis, electrodeionization, photocatalysis and nanotechnology: A review, *Environ. Chem. Lett.*, 18(2020), No. 6, p. 2055.

[20] A. Shishov, P. Terno, L. Moskvin, and A. Bulatov, In-syringe dispersive liquid-liquid microextraction using deep eutectic solvent as disperser: Determination of chromium (VI) in beverages, *Talanta*, 206(2020), art. No. 120209.
[21] H.M. Xu, J.F. Wei, and X.L. Wang, Nanofiltration hollow fiber membranes with high charge density prepared by simultaneous electron beam radiation-induced graft polymerization for removal of Cr(VI), *Desalination*, 346(2014), p. 122.
[22] K.G. Pavithra, P.S. Kumar, F.C. Christopher, and A. Saravanan, Removal of toxic Cr(VI) ions from tannery industrial wastewater using a newly designed three-phase three-dimensional electrode reactor, *J. Phys. Chem. Solids*, 110(2017), p. 379.
[23] M. Imron, S.B. Kurniawan, and I. Purwanti, Biosorption of chromium by living cells of azotobacter S8, bacillus subtilis and pseudomonas aeruginosa using batch system reactor, *J. Ecol. Eng.*, 20(2019), No. 6, p. 184.
[24] X. Duan, R. Lv, and Z. Kong, An anionic metal–organic framework for selective adsorption separation toward methylene blue and rhodamine B, *Z. Anorg. Allg. Chem.*, 646(2020), No. 17, p. 1408.
[25] X. Duan, R. Lv, S. Li, J.X. Tang, J.Y. Ge, and D. Zhao, Two –COOH decorated anionic metal–organic frameworks with open Cu^{2+} sites afforded highly C_2H_2/CO_2 and C_2H_2/CH_4 separation and removal of organic dyes, *Z. Anorg. Allg. Chem.*, 645(2019), No. 14, p. 955.
[26] F.J. Zheng, Z.Y. Ren, B. Xu, *et al*., Elucidating multiple-scale reaction behaviors of phenolic resin pyrolysis via TG-FTIR and ReaxFF molecular dynamics simulations, *J. Anal. Appl. Pyrolysis*, 157(2021), art. No. 105222.
[27] T. Ahamad and S.M. Alshehri, Thermal degradation and evolved gas analysis: A polymeric blend of urea formaldehyde (UF) and epoxy (DGEBA) resin, *Arab. J. Chem.*, 7(2014), No. 6, p. 1140.
[28] S.Q. Wang, H. Chen, and X.M. Zhang, Transformation of aromatic structure of vitrinite with different coal ranks by HRTEM *in situ* heating, *Fuel*, 260(2020), art. No. 116309.
[29] S. Rodrigues, I. Suárez-Ruiz, M. Marques, I. Camean, and D. Flores, Microstructural evolution of high temperature treated anthracites of different rank, *Int. J. Coal Geol.*, 87(2011), No. 3-4, p. 204.
[30] G.S. Jiang, M.L. Chen, Y.Z. Sun, and J.Q. Pan, Dual N-doped porous carbon derived from pyrolytic carbon black and critical PANIs constructing high-performance Zn ion hybrid supercapacitor, *J. Energy Storage*, 63(2023), art. No. 106955.
[31] J. Liang, X.G. Duan, X.Y. Xu, *et al*., Biomass-derived pyrolytic carbons accelerated Fe(III)/Fe(II) redox cycle for persulfate activation: Pyrolysis temperature-depended performance and mechanisms, *Appl. Catal. B*, 297(2021), art. No. 120446.
[32] S.A. Fahad, M.S. Nawab, M.A. Shaida, *et al*., Carbon based adsorbents for the removal of U(VI) from aqueous medium: A state of the art review, *J. Water Process. Eng.*, 52(2023), art. No. 103458.
[33] A.S. Yusuff, M.A. Lala, K.A. Thompson-Yusuff, and E.O. Babatunde, $ZnCl_2$-modified eucalyptus bark biochar as adsorbent: Preparation, characterization and its application in adsorption of Cr(VI) from aqueous solutions, *S. Afr. J. Chem. Eng.*, 42(2022), p. 138.
[34] G. Abdul, X.Y. Zhu, and B.L. Chen, Structural characteristics of biochar-graphene nanosheet composites and their adsorption performance for phthalic acid esters, *Chem. Eng. J.*, 319(2017), p. 9.
[35] L.X. Zhang, S.Y. Tang, F.X. He, Y. Liu, W. Mao, and Y.T. Guan, Highly efficient and selective capture of heavy metals by poly(acrylic acid) grafted chitosan and biochar composite for wastewater treatment, *Chem. Eng. J.*, 378(2019), art. No. 122215.
[36] A.S. Yusuff, Adsorption of hexavalent chromium from aqueous solution by *Leucaena leucocephala* seed pod activated carbon: Equilibrium, kinetic and thermodynamic studies, *Arab J. Basic Appl. Sci.*, 26(2019), No. 1, p. 89.
[37] S.Z. Xu, S.Y. Ning, Wang Y., *et al*., Precise separation and efficient enrichment of palladium from wastewater by amino-functionalized silica adsorbent, *J. Cleaner Prod.*, 396(2023), art. No. 136479.
[38] X. Tao, F.X. Chen, J. Li, Y.L. Liu, X.W. Hu, and R. Chen, Efficient promotion of Cr(VI) removal over Bi_2S_3 nanoparticles with cupric ions: Potential applications in electroplating wastewater and contaminated groundwater, *Sep. Purif. Technol.*, 303(2022), art. No. 122114.
[39] M. Pourrahmati-Shiraz, A. Mohagheghian, and M. Shirzad-Siboni, Synthesis of ZnO immobilized on recycled polyethylene terephtalate for sonocatalytic removal of Cr(VI) from synthetic, drinking waters and electroplating wastewater, *J. Environ. Manage.*, 324(2022), art. No. 116395.
[40] Y.N. He, J.B. Chen, J.P. Lv, *et al*., Separable amino-functionalized biochar/alginate beads for efficient removal of Cr(VI) from original electroplating wastewater at room temperature, *J. Cleaner Prod.*, 373(2022), art. No. 133790.
[41] A.P. LaGrow, M.O. Besenhard, A. Hodzic, *et al*., Unravelling the growth mechanism of the co-precipitation of iron oxide nanoparticles with the aid of synchrotron X-ray diffraction in solution, *Nanoscale*, 11(2019), No. 14, p. 6620.
[42] Y. Ding, N.T.H. Nhung, J. An, *et al*., Manganese–titanium mixed ion sieves for the selective adsorption of lithium ions from an artificial salt lake brine, *Materials*, 16(2023), No. 11, art. No. 4190.
[43] M. Islam, M. Angove, D. Morton, B. Pramanik, and M. R. Awual, A mechanistic approach of chromium (VI) adsorption onto manganese oxides and boehmite, *J. Environ. Chem. Eng.*, 8(2020), art. No. 103515.
[44] H.Y. Li, N. Li, P.P. Zuo, S.J. Qu, and W.Z. Shen, Efficient adsorption-reduction synergistic effects of sulfur, nitrogen and oxygen heteroatom co-doped porous carbon spheres for chromium(VI) removal, *Colloids Surf. A*, 618(2021), art. No. 126502.
[45] A. Pholosi, E.B. Naidoo, and A.E. Ofomaja, Intraparticle diffusion of Cr(VI) through biomass and magnetite coated biomass: A comparative kinetic and diffusion study, *S. Afr. J. Chem. Eng.*, 32(2020), p. 39.
[46] B. Ghanim, T.F. O'Dwyer, J.J. Leahy, *et al*., Application of KOH modified seaweed hydrochar as a biosorbent of vanadium from aqueous solution: Characterisations, mechanisms and regeneration capacity, *J. Environ. Chem. Eng.*, 8(2020), No. 5, art. No. 104176.
[47] K. Yang, J. Xing, P. Xu, J. Chang, Q. Zhang, and K.M. Usman, Activated carbon microsphere from sodium lignosulfonate for Cr(VI) adsorption evaluation in wastewater treatment, *Polymers*, 12(2020), No. 1, art. No. 236.
[48] Y.Y. Sun, C. Liu, Y.F. Zan, G. Miao, H. Wang, and L.Z. Kong, Hydrothermal carbonization of microalgae (chlorococcum sp.) for porous carbons with high Cr(VI) adsorption performance, *Appl. Biochem. Biotechnol.*, 186(2018), No. 2, p. 414.
[49] H.J. Xu, Y.X. Liu, H.X. Liang, *et al*., Adsorption of Cr(VI) from aqueous solutions using novel activated carbon spheres derived from glucose and sodium dodecylbenzene sulfonate, *Sci. Total Environ.*, 759(2021), art. No. 143457.
[50] R.H. Huang, B.C. Yang, Q. Liu, and Y.P. Liu, Multifunctional activated carbon/chitosan composite preparation and its simultaneous adsorption of phenol and Cr(VI) from aqueous solutions, *Environ. Prog. Sustainable Energy*, 33(2014), No. 3, p. 814.
[51] Z. Al-Qodah, R. Dweiri, M. Khader, *et al*., Processing and characterization of magnetic composites of activated carbon, fly ash, and beach sand as adsorbents for Cr(VI) removal, *Case Stud. Chem. Environ. Eng.*, 7(2023), art. No. 100333.

[52] M.K. Rajput, R. Hazarika, and D. Sarma, Zerovalent iron decorated tea waste derived porous biochar [ZVI@TBC] as an efficient adsorbent for Cd(II) and Cr(VI) removal, *J. Environ. Chem. Eng.*, 11(2023), No. 4, art. No. 110279.
[53] Z.M. Sun, B.X. Liu, M.Z. Li, C.Q. Li, and S.L. Zheng, Carboxyl-rich carbon nanocomposite based on natural diatomite as adsorbent for efficient removal of Cr(VI), *J. Mater. Res. Technol.*, 9(2020), No. 1, p. 948.
[54] K.Y. Liu, D.Y. Zhao, Z.F. Hu, *et al*., The adsorption and reduction of anionic Cr(VI) in groundwater by novel iron carbide loaded on N-doped carbon nanotubes: Effects of Fe-confinement, *Chem. Eng. J.*, 452(2023), art. No. 139357.
[55] Z.Y. Kang, H. Gao, Z.L. Hu, X.D. Jia, and D.S. Wen, Ni-Fe/reduced graphene oxide nanocomposites for hexavalent chromium reduction in an aqueous environment, *ACS Omega*, 7(2022), No. 5, p. 4041.
[56] Z. Liu, J.Y. Luo, Y. Peng, Y.H. Yang, Z. Zeng, and L.Q. Li, Preparation of phosphorus-containing porous carbon by direct carbonization for acetone adsorption, *Colloids Surf. A*, 606(2020), art. No. 125431.
[57] S.I. Lyubchik, A.I. Lyubchik, O.L. Galushko, *et al*., Kinetics and thermodynamics of the Cr(III) adsorption on the activated carbon from co-mingled wastes, *Colloids Surf. A*, 242(2004), No. 1-3, p. 151.
[58] W. Ahmed, S. Mehmood, A. Núñez-Delgado, *et al*., Enhanced adsorption of aqueous Pb(II) by modified biochar produced through pyrolysis of watermelon seeds, *Sci. Total Environ.*, 784(2021), art. No. 147136.
[59] W. Ahmad, A.S. Bashammakh, A.A. Al-Sibaai, H. Alwael, and M.S. El-Shahawi, Trace determination of Cr(III) and Cr(VI) species in water samples via dispersive liquid–liquid microextraction and microvolume UV–Vis spectrometry. Thermodynamics, speciation study, *J. Mol. Liq.*, 224(2016), p. 1242.
[60] J.J. Chai, Q. Hu, and B. Qiu, Conductive polyaniline improves Cr(VI) bio-reduction by anaerobic granular sludge, *Adv. Compos. Hybrid Mater.*, 4(2021), No. 4, p. 1137.
[61] R.Q. Li, D. Hu, K. Hu, *et al*., Coupling adsorption-photocatalytic reduction of Cr(VI) by metal-free N-doped carbon, *Sci. Total Environ.*, 704(2020), art. No. 135284.
[62] Q.Q. Tang, H. Wu, M.S. Zhou, and D.J. Yang, Preparation of a novel high-performance lignin-based anionic adsorption resin for efficient removal of Cr(VI) in aqueous solutions, *Ind. Crops Prod.*, 199(2023), art. No. 116720.
[63] L. Guo, Y.F. Zhang, J.J. Zheng, *et al*., Synthesis and characterization of ZnNiCr-layered double hydroxides with high adsorption activities for Cr(VI), *Adv. Compos. Hybrid Mater.*, 4(2021), No. 3, p. 819.
[64] X. Dai, N.T.H. Nhung, M.F. Hamza, *et al*., Selective adsorption and recovery of scandium from red mud leachate by using phosphoric acid pre-treated pitaya peel biochar, *Sep. Purif. Technol.*, 292(2022), art. No. 121043.
[65] W. Li, L.F. Chai, B.Y. Du, X.H. Chen, and R.C. Sun, Full-lignin-based adsorbent for removal of Cr(VI) from waste water, *Sep. Purif. Technol.*, 306(2023), art. No. 122644.
[66] Z.H. Yang, L.L. Ren, L.F. Jin, *et al., In-situ* functionalization of poly(m-phenylenediamine) nanoparticles on bacterial cellulose for chromium removal, *Chem. Eng. J.*, 344(2018), p. 441.
[67] M.Y. Zhang, L.H. Song, H.F. Jiang, *et al*., Biomass based hydrogel as an adsorbent for the fast removal of heavy metal ions from aqueous solutions, *J. Mater. Chem. A*, 5(2017), No. 7, p. 3434.